J Mater Sci (2020) 55:15152–15166

Chemical routes to materials

Late-model g-CNQDs/$H_3PW_{12}O_{40}$/TiO_2 heterojunction nanocatalyst with enhanced photocatalytic performance

Tingting Sun[1], Xinmin Yu[1], Shaowei Zhong[1], Lei Xu[1,*], and Yahui Zhao[2,*]

[1] School of Chemistry and Environmental Engineering, Changchun University of Science and Technology, Changchun 130022, People's Republic of China

[2] School of Environment, Northeast Normal University, Changchun 130024, People's Republic of China

Received: 25 April 2020
Accepted: 18 July 2020
Published online: 28 July 2020

ABSTRACT

The g-CNQDs/$H_3PW_{12}O_{40}$/TiO_2 heterojunction photocatalytic material is fabricated by facile ultrasonic method. The crystal structure, elemental composition, morphology and optical properties of as-synthesized catalysts are investigated by a series of characterizations. Studies have shown that g-CNQDs have been successfully doped into $H_3PW_{12}O_{40}$/TiO_2. The introduced g-CNQDs are uniform in size and have an average diameter of 5.8 nm. The 5% g-CNQDs/$H_3PW_{12}O_{40}$/TiO_2 shows the highest degradation efficiency of 99.3% toward RhB under simulated sunlight for 30 min, which is 5.68 times than of $H_3PW_{12}O_{40}$/TiO_2 under same conditions. The improved photocatalytic activity of the g-CNQDs/$H_3PW_{12}O_{40}$/TiO_2 ternary system is attributed to the expansion of visible-light absorption region and diminishing photoelectron–hole recombination. The testing of radical scavengers demonstrated that the main active species in the photocatalytic process involving three active species are $\cdot O_2^-$ and $\cdot OH$, and the holes (h_{VB}^+) play an auxiliary role. The photodegradation efficiency of g-CNQDs/$H_3PW_{12}O_{40}$/TiO_2 ternary composite catalyst is reduced by 6.2% after five cycling runs. The present work proposes an efficient optimization of the fabrication of potent and stable TiO_2-based photocatalysts driven by sunlight.

Address correspondence to E-mail: xul646@163.com; zhaoyh246@nenu.edu.cn

https://doi.org/10.1007/s10853-020-05083-7

GRAPHIC ABSTRACT

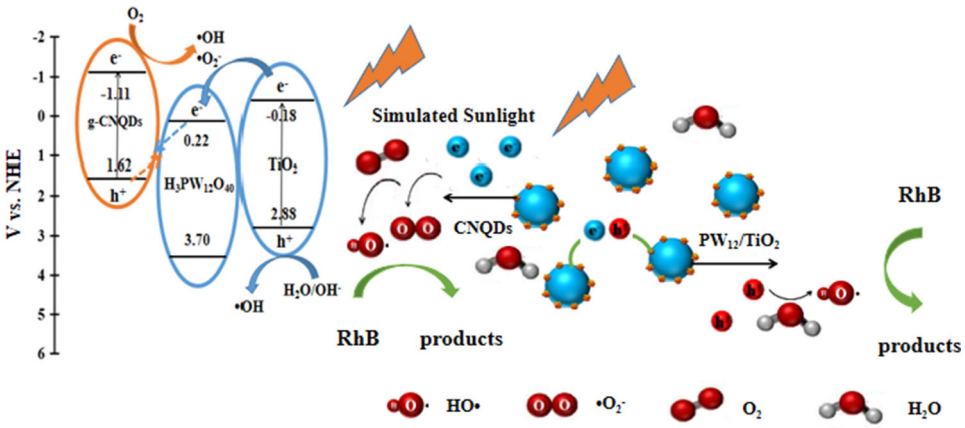

Introduction

The exploitation of semiconductor photocatalysts driven by sunlight has become a trend to mitigate the energy and environment situation [1–5]. TiO_2 photocatalyst is popular for degrading organic contaminants in virtue of oxidation power, stability, low cost and non-toxic. However, the practical application of TiO_2 remains limited due to poor quantum yield and wide bandgap [6, 7]. Up to now, numerous strategies have been demonstrated to boost the catalytic activity of TiO_2. Among them, the design of TiO_2-based heterostructures [8–11] has been a feasible and efficient strategy to surmount the shortcomings of fast photoinduced carriers' recombination and restricted visible-light response of TiO_2. Yi et al. [12] demonstrated that $Bi_2Ti_2O_7/TiO_2$ heterostructures with higher photodegradation efficiency are attributed to enhanced light-harvesting and efficient carrier transfer. Nevertheless, the construction of TiO_2-based photocatalytic materials still exists restriction in degrading organic contaminants.

Graphitic carbon nitride (g-C_3N_4) is a class of metal-free photocatalyst with a narrow bandgap of 2.70 eV, which allows it to absorb visible-light without modification [13]. G-C_3N_4 exhibits superiority in terms of photodegradation of organic contaminants and hydrogen production by water decomposition [14]. However, currently available g-C_3N_4 materials are typically sub-micrometer sized. Low dimensionalization of g-C_3N_4 forms g-C_3N_4 quantum dots (abbreviated as g-CNQDs), which possess up-conversion luminescence effect [15–20]. Howbeit, it has limited efficiency of directly utilize g-CNQDs for organic contaminants photodegradation. To build a composite system with g-CNQDs and other vectors, we utilized the up-conversion characteristics of g-CNQDs to convert long-wave illumination light into shorter-wavelength emission light for composite materials [21]. Meanwhile, the heterojunction generated after recombination can facilitate photoinduced carriers' separation. Accordingly, it would contribute to the development of g-CNQDs load materials for photocatalytic applications. Many reports focused on various loaded g-CNQDs heterostructures lately, such as g-CNQDs/g-C_3N_4, g-CNQDs/graphene and $BiVO_4$/CNQDs/NCDs [22–24]. Su et al. [25] confirmed that g-CNQDs/TiO_2 nanotube arrays (NTAs) heterojunction displays better photocatalytic performance in the decomposition of rhodamine B (RhB) and put it down to enhanced light absorption and the migration of light-excited electrons from g-CNQDs to TiO_2. Nevertheless, the photodegradation efficiency of g-CNQDs/TiO_2 needs to go one step further.

Herein, we carried on a successful attempt at the preparation of g-CNQDs/$H_3PW_{12}O_{40}$/TiO_2 ternary hybrids via coupling g-CNQDs with $H_3PW_{12}O_{40}$/TiO_2 by facile ultrasonic method. The introduction of g-CNQDs and $H_3PW_{12}O_{40}$ significantly boosts the photocatalytic activity of TiO_2. $H_3PW_{12}O_{40}$, as one type of significant transition metal-oxide clusters with multiple topologies and high valence negative ion charges, has been considered as a dual-function green catalyst with redox characteristics and electron capture capacity [26, 27]. $H_3PW_{12}O_{40}$ combines with TiO_2 can diminish photogenerated carriers' recombination rate in virtue of the outstanding electron acceptability of Keggin units [28]. In terms of $H_3PW_{12}O_{40}$/TiO_2 composite, the restricted UV-light response results in a corresponding low solar utilization. In this context, we further doped g-CNQDs to construct g-CNQDs/$H_3PW_{12}O_{40}$/TiO_2 heterostructure stems from several considerations: (1) wide bandgap semiconductor coupled with narrow bandgap semiconductor can effectively enhance its visible-light absorption owing to the synergic absorption effect in a heterojunction. (2) matching band edge position among distinct materials greatly facilitates the separation and transmission of photoinduced electron–hole, thereby increasing quantum efficiency. (3) the up-conversion effect of g-CNQDs increases UV-light intensity to some extent. The crystal structure, elemental composition, morphology and optical properties of as-synthesized catalysts were characterized. The catalytic activity of ternary composite was assessed by measuring the decomposition of RhB under simulated sunlight ($320\ \text{nm} < \lambda < 780\ \text{nm}$). And then the photodegradation reactions of TiO_2, g-CNQDs, $H_3PW_{12}O_{40}$/TiO_2, g-CNQDs/TiO_2 were also compared. Photoluminescence (PL) analysis and photoelectrochemistry (PEC) measurements were performed to disclose the migration and separation efficiency of light-excited charge carriers among composite materials. Beyond that, the active species formed in the process of photodegradation were the possible reaction mechanism of g-CNQDs/$H_3PW_{12}O_{40}$/TiO_2 system. Last but not least, we made recycling experiments to validate the stability and reusability of the ternary composite under identical reaction conditions.

Experimental section

Preparation of g-CNQDs

Solid-phase reaction method: 1.01 g of urea and 0.81 g of sodium citrate were first placed in an agate mortar and continuously ground for half an hour before placed in a high temperature reaction kettle and then placed the mixture in a temperature-programmed box and heated to 180 °C for 1 h. After taking out, it was cooled to room temperature and then dried in a dry box for 6 h to obtain a g-C_3N_4 nano material. Next, the obtained g-C_3N_4 nanomaterial was ground into powder using a mortar and centrifuged at 8000 rpm for 10 min with ethanol dispersion. The procedure was repeated three times to remove some unreacted precursor, and finally, the obtained solid was charged into 1000 Da. The dialysis bag was dialyzed in water for 24 h, and the obtained product was freeze-dried for 24 h to obtain pure g-CNQDs material.

Preparation of g-CNQDs/$H_3PW_{12}O_{40}$/TiO_2

The fabrication of $H_3PW_{12}O_{40}$/TiO_2 was conducted by sol–gel method following the literature [29]. A certain amount of $H_3PW_{12}O_{40}$/TiO_2 binary catalyst powder and g-CNQDs powder were weighed and mixed well, and the mixture was added to 30 mL distilled water. The suspension was stirred for 30 min and ultrasound for another 30 min. The above process repeated twice. The obtained solution was allowed to settle in a closed and dry environment for 12 h. The mixed solution was placed in a constant temperature drying oven and dried at 80 °C for 12 h, and then fully ground into powder to obtain a g-CNQDs/$H_3PW_{12}O_{40}$/TiO_2 ternary composite catalyst. The mass ratio of g-CNQDs to $H_3PW_{12}O_{40}$/TiO_2 was 3%, 5% and 10%, respectively.

Catalyst characterizations

The crystalline structure of as-synthesized samples was presented on Ricoh Y-2000 X-ray powder diffractometer. The FTIR spectrum texts were actualized on Nicolet 360 spectrometer with distinct samples dispersed in KBr desiccative. Transmission electron microscopy (TEM) images were acquired on JEOL Hitachi-600. X-ray photoelectron spectroscopes (XPS) were measured on a VG-ADES 400IR

spectrometer with Mg K-ADES source at a residual gas pressure that below 10^{-8} Pa. The resolution limitation of XPS is 0.65 eV. UV–vis absorption spectra were obtained using a Cary 500 UV–vis–NIR spectrophotometer. The specific surface areas and pore size distribution of catalysts are determined by V-SORB2802 analyzer at 77 K. PL spectra of distinct samples are conducted on FL 7000 fluorescence spectrometer at room temperature. Photocurrent experiments were actualized on CHI 630E electrochemical station.

Photocatalytic experiments

The photocatalytic activity of g-CNQDs/$H_3PW_{12}O_{40}/TiO_2$ composite was investigated by degrading RhB. The photocatalyst (50 mg) was added to aqueous solution of RhB (50 mL, 20 mg L^{-1}). Prior to the start of the photocatalytic experiment, the solution was mechanically stirred for a certain time to achieve adsorption–desorption equilibrium. Then, we turn on the xenon lamp to simulate sunlight source and stirring was continued throughout the reaction to bring the catalyst into full contact with the RhB solution. Samples were taken every 5 min and the samples were immediately filtered through a 0.22 μm pinhole filter to remove the catalyst. The absorbance of each sample was measured by a UV–Vis spectrophotometer at 553 nm, and the degradation rate was converted by the absorbance ratio.

Results and discussion

Characterization

Figure 1 exhibits the XRD patterns of as-synthesized catalysts. The anatase TiO_2 standard cards have diffraction peaks at 25.4° (101), 38.1° (004), 48.0° (200), 54.0° (105) and 55.2° (211), respectively (JCPDS No. 21-1272). The catalysts containing TiO_2 in the figure have identical characteristic diffraction peaks of anatase crystal form, which indicates that the TiO_2 in the composite prepared by sol–gel method belongs to anatase phase [30]. The doping amount of $H_3PW_{12}O_{40}$ or g-CNQDs does not change its crystalline structure. No characteristic diffraction peak of $H_3PW_{12}O_{40}$ can be observed, since only a small amount of $H_3PW_{12}O_{40}$ content distributed in TiO_2

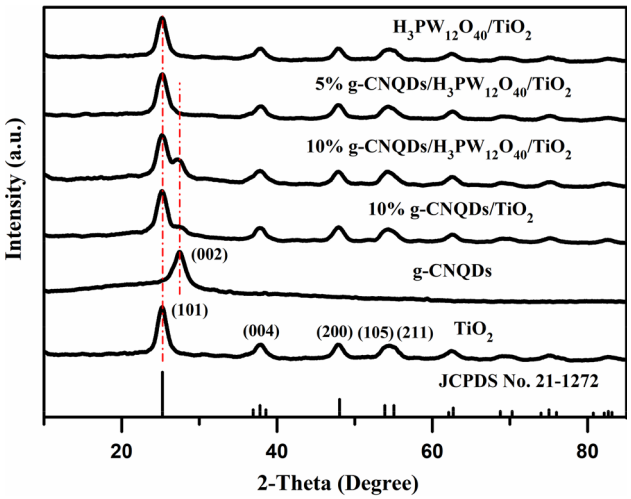

Figure 1 XRD patterns of as-synthesized TiO_2, g-CNQDs, $H_3PW_{12}O_{40}/TiO_2$, 10% g-CNQDs/TiO_2, 5% g-CNQDs/$H_3PW_{12}O_{40}/TiO_2$, 10% g-CNQDs/$H_3PW_{12}O_{40}/TiO_2$.

material. For pure g-CNQDs, 27.2° (d = 0.336 nm) corresponds to the (002) plane of hexagonal graphitic C_3N_4 (JCPDS No. 87-1526) [31]. This indicates that the fabricated g-CNQDs have graphite phase crystal forms. No characteristic peak of g-CNQDs can be observed in 5% g-CNQDs/$H_3PW_{12}O_{40}/TiO_2$, which may due to the relatively small doping amount of g-CNQDs. The 10% g-CNQDs/$H_3PW_{12}O_{40}/TiO_2$ shows a characteristic peak of g-CNQDs at 27.2°, which indicates that g-CNQDs has been successfully loaded into $H_3PW_{12}O_{40}/TiO_2$. In 10% g-CNQDs/TiO_2, characteristic peaks of TiO_2 and g-CNQDs appear simultaneously as well.

As shown in Fig. 2, the prepared TiO_2, $H_3PW_{12}O_{40}$, g-CNQDs, $H_3PW_{12}O_{40}/TiO_2$, 10% g-CNQDs/TiO_2 and 10% g-CNQDs/$H_3PW_{12}O_{40}/TiO_2$ catalysts are subjected to FTIR test analysis. For pure TiO_2, the characteristic peak at 450.4 cm^{-1} is assigned to Ti–O–Ti bond stretching vibration in anatase crystals [32]. In the FTIR spectrum of g-CNQDs, the peak at 803 cm^{-1} is attributed to the CN heterocycle of triazine units in g-CNQDs [33]. Several strong characteristic peaks at 1237, 1317, 1411, 1470, 1565 and 1638 cm^{-1} correspond to the typical stretching modes of CN heterocycle [34, 35]. A broad absorption band from 3100 to 3400 cm^{-1} represents NH groups' stretching vibration [36]. The characteristic peaks of TiO_2 and g-CNQDs appear simultaneously in the composites g-CNQDs/TiO_2 and g-CNQDs/$H_3PW_{12}O_{40}/TiO_2$, indicating that g-CNQDs have been successfully loaded into the target material. In

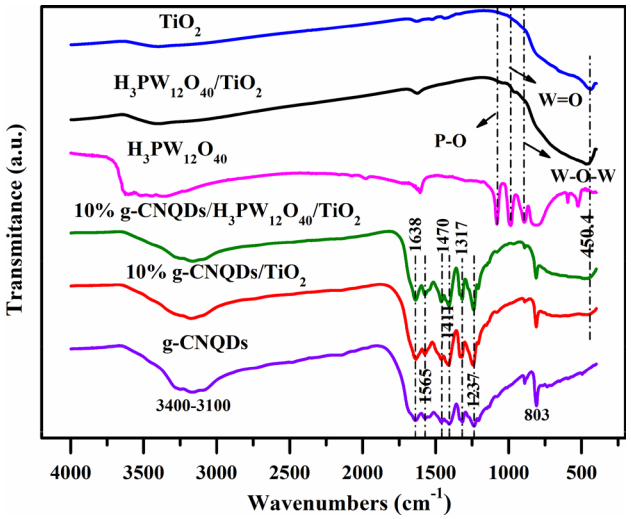

Figure 2 FT-IR spectra of TiO_2, $H_3PW_{12}O_{40}$, g-CNQDs, $H_3PW_{12}O_{40}/TiO_2$, 10% g-CNQDs/TiO_2, 10% g-CNQDs/$H_3PW_{12}O_{40}/TiO_2$.

addition, the vibration absorption peak positions of the P–O, W=O and W–O–W bonds should be at 1085, 962 and 893 cm^{-1}, respectively [37, 38]. However, these characteristic peaks are weak in $H_3PW_{12}O_{40}/TiO_2$ and 10% g-CNQDs/$H_3PW_{12}O_{40}/TiO_2$ due to the low dosage of $H_3PW_{12}O_{40}$.

XPS is used to detect the chemical composition of the surface and determines the chemical state of each element of as-prepared catalysts. The survey spectrum in Fig. 3a reveals the presence of C, N for g-CNQDs; Ti, O, W for $H_3PW_{12}O_{40}/TiO_2$; C, N, Ti, O, W for g-CNQDs/$H_3PW_{12}O_{40}/TiO_2$ composite. Figure 3b shows the high-resolution XPS spectrum of C1s. The peaks at 284.6 eV and 287.6 eV in g-CNQDs are derived from sp^2-hybridized carbon atoms in graphite phase and sp^3-bonded carbon in C-N of g-CNQDs [39]. As shown in Fig. 3c, the N 1*s* peak in g-CNQDs can be divided into two peaks at 398.4 eV and 399.9 eV, which are assigned to triazine rings (C–N–C) and tertiary nitrogen ($N–C_3$), respectively [40]. The binding energy values in 5% g-CNQDs/$H_3PW_{12}O_{40}/TiO_2$ (288.1 eV, 398.6 eV and 400.0 eV) exhibit certain positive displacements in contrast to those of C, N in g-CNQDs (287.6 eV, 398.4 eV and 399.9 eV), which indicates robust interaction among composite materials. Figure 3d shows the XPS spectrum of O1s where three characteristic peaks appear at 529.7 eV, 531.4 eV and 532.8 eV, respectively. The peaks at 529.7 eV and 531.4 eV belong to lattice oxygen of anatase TiO_2 and Keggin unit of $H_3PW_{12}O_{40}$, and the physical-absorption water of 532.8 eV [41]. Compared to $H_3PW_{12}O_{40}/TiO_2$ (529.8 eV, 531.7 eV), the binding energy values of oxygen in g-CNQDs/$H_3PW_{12}O_{40}/TiO_2$ (529.7 eV, 531.4 eV) show negative deviations, implying the interaction between g-CNQDs and $H_3PW_{12}O_{40}/TiO_2$. As shown in Fig. 3e, the peaks located at 458.4 eV and 464.0 eV correspond to Ti $2p_{3/2}$ and Ti $2p_{1/2}$, respectively, which indicates that Ti element presents in the form of high-value oxidation state Ti^{4+} [42]. The binding energy value of titanium in 5% g-CNQDs/$H_3PW_{12}O_{40}/TiO_2$ (464.4 eV) increases 0.2 eV in comparison with that of $H_3PW_{12}O_{40}/TiO_2$ (464.2 eV), further confirmed the interaction between g-CNQDs and $H_3PW_{12}O_{40}/TiO_2$ in the composite. In Fig. 3f, we can see that the peaks located at 34.80 eV and 36.80 eV relate to W $4f_{7/2}$ and W $4f_{5/2}$, respectively, and the W element has the highest oxidation state [W(VI)] [43]. It is notable that the O, Ti and W binding energies in $H_3PW_{12}O_{40}/TiO_2$ display certain displacements than those of pure TiO_2 and $H_3PW_{12}O_{40}$, which confirms the formation of Ti–O–W chemical bonds [44]. Due to the low content of P element in $H_3PW_{12}O_{40}/TiO_2$, it is not detected by the machine. The above results indicate that $H_3PW_{12}O_{40}/TiO_2$ is successfully combined with g-CNQDs.

The TEM researches the morphology of as-synthesized catalysts. In order to control the morphology and size of g-CNQDs, three methods, acid etching, evaporation condensation and solid-state reaction, were used to prepare g-CNQDs. As shown in Figure S1 (a–c), the morphology and size of g-CNQDs prepared by solid-phase reaction method are very uniform. Therefore, the solid-state reaction method was selected as the method of preparing g-CNQDs. The carbon nitride quantum dots are well dispersed and uniform in size, and the particle sizes are mostly around 3–9 nm with an average size of 5.8 nm (Fig. 4a and S1d). $H_3PW_{12}O_{40}/TiO_2$ has a particle size of about 10–-0 nm (Fig. 4b). It can be observed that g-CNQDs are loaded on the surface of $H_3PW_{12}O_{40}/TiO_2$ composite (Fig. 4c). By measuring the lattice fringes in Fig. 4d, the interplanar distances are approximately 0.353 nm and 0.336 nm, corresponding to the (101) plane of anatase TiO_2 and the (002) plane of g-CNQDs, respectively. Their close combination demonstrates the formation of a heterojunction between g-CNQDs and TiO_2.

The N_2 adsorption–desorption isotherms of g-CNQDs, $H_3PW_{12}O_{40}/TiO_2$ and 5% g-CNQDs/

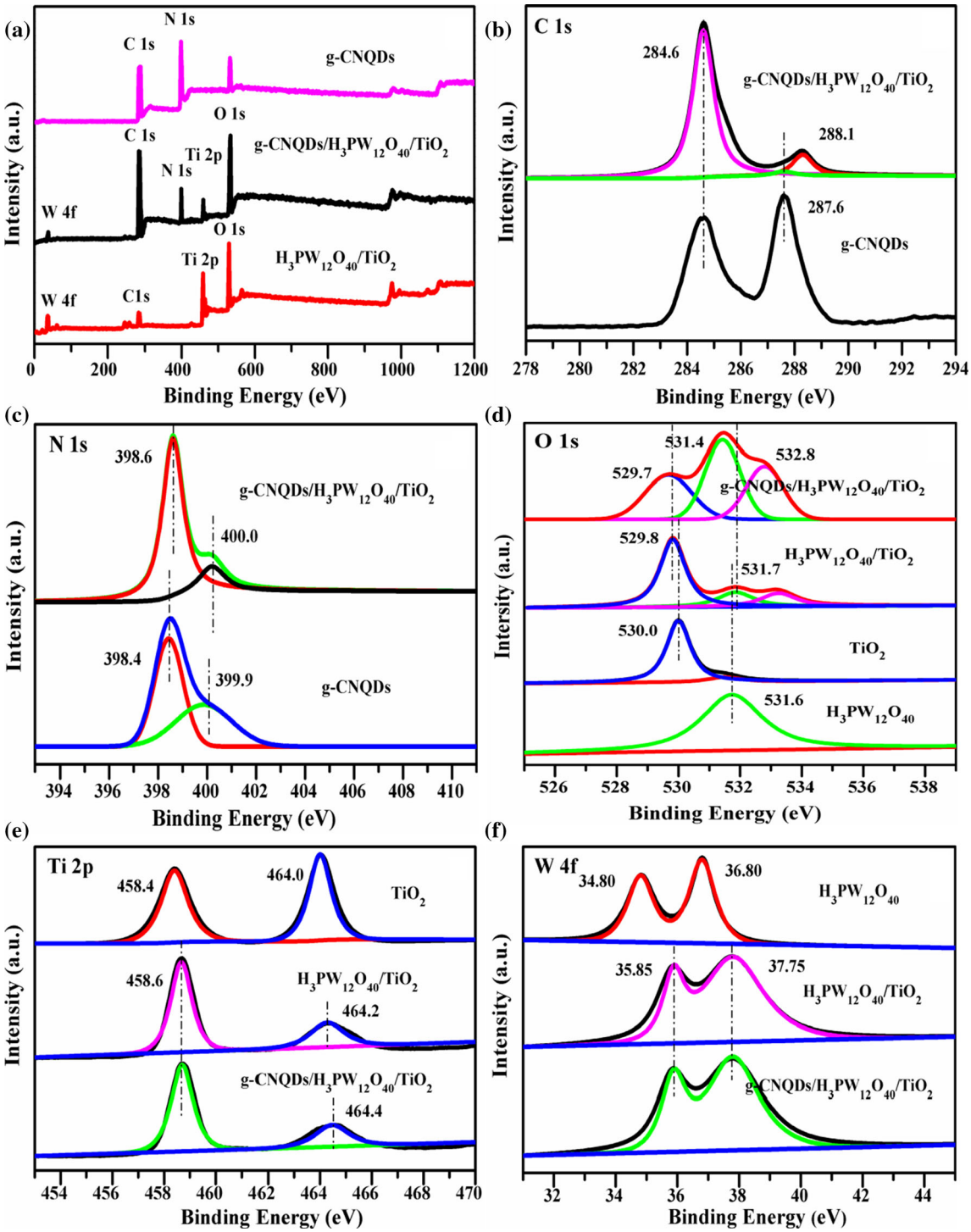

Figure 3 XPS spectrum of g-CNQDs, $H_3PW_{12}O_{40}/TiO_2$, 5% g-CNQDs/$H_3PW_{12}O_{40}/TiO_2$, **a** survey, **b** C 1*s*, **c** N 1*s*, **d** O 1*s*, **e** Ti 2*p*, **f** W 4*f*.

$H_3PW_{12}O_{40}/TiO_2$ are shown in Fig. S2. The g-CNQDs show type-IV isotherms with H3 hysteresis loop according to the IUPAC classification, which is related to the characteristic capillary condensation within the mesopore channels. The BET surface areas of g-CNQDs, $H_3PW_{12}O_{40}/TiO_2$ and 5% g-CNQDs/$H_3PW_{12}O_{40}/TiO_2$ are 184.6, 72.2 and 94.3 m^2/g, respectively. In comparison with $H_3PW_{12}O_{40}/TiO_2$,

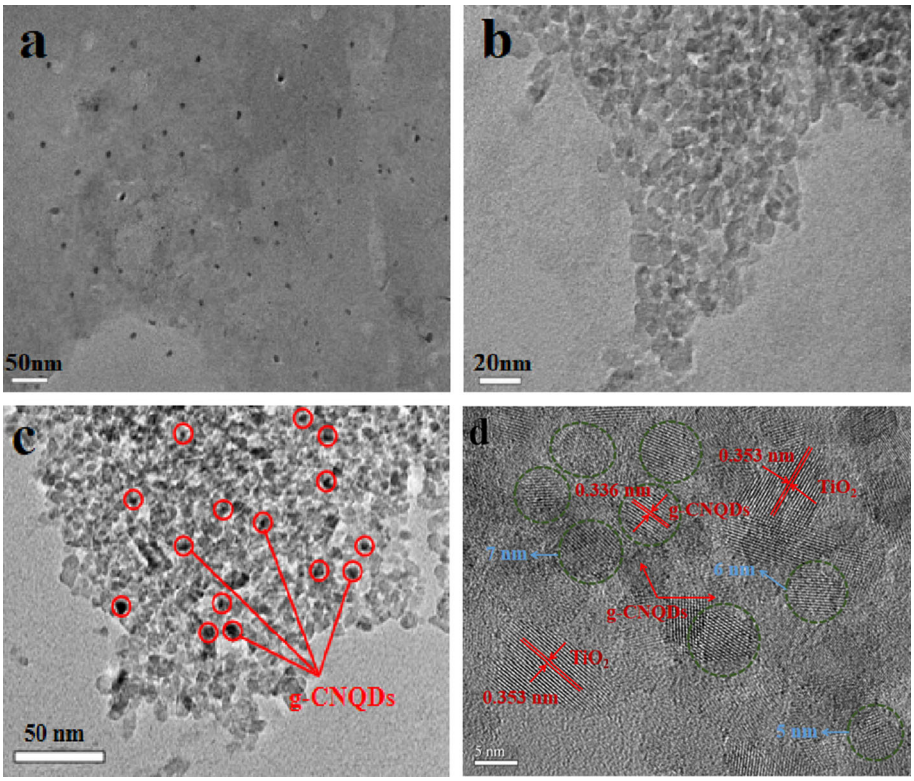

Figure 4 TEM image of **a** g-CNQDs, **b** $H_3PW_{12}O_{40}/TiO_2$, **c** g-CNQDs/$H_3PW_{12}O_{40}/TiO_2$, HRTEM image of **d** g-CNQDs/$H_3PW_{12}O_{40}/TiO_2$.

the larger surface area of g-CNQDs/$H_3PW_{12}O_{40}/TiO_2$ is expected to provide more active sites for photocatalytic reaction.

The optical properties of photocatalyst exert a significant function in determining its photocatalytic performance toward organic contaminants. The light absorption capacity of as-prepared samples is measured by UV–Vis DRS (Fig. 5). For g-CNQDs, the absorption boundary is approximately 450 nm, and the bandgap is estimated to be 2.73 eV, which is consistent with previous reports [45]. Due to the influence of g-CNQDs quantum size effect, it is blueshifted relative to g-C_3N_4 (Fig. S3). There is a strong absorption region of TiO_2 among 200–400 nm in virtue of the electronic transition from O 2*p* orbitals to Ti 2*p* orbitals [46]. The absorption boundary of $H_3PW_{12}O_{40}/TiO_2$ has a blueshift compared with TiO_2, which is attributed to the smaller particle size of $H_3PW_{12}O_{40}/TiO_2$ [47]. 5% g-CNQDs/TiO_2 redshifted compared to pure TiO_2, due to the electronic interaction between TiO_2 and g-CNQDs. 5% g-CNQDs/$H_3PW_{12}O_{40}/TiO_2$ redshifted as well, indicating higher separation efficiency of photoinduced carriers. The bandgap energy of 5% g-CNQDs/TiO_2 and 5% g-CNQDs/$H_3PW_{12}O_{40}/TiO_2$ composite catalysts is gradually reduced, which improved the photon efficiency of the system. According to the Kubelka–Munk function [48], the bandgaps of g-CNQDs, TiO_2, $H_3PW_{12}O_{40}/TiO_2$, 5% g-CNQDs/TiO_2 and 5% g-CNQDs/$H_3PW_{12}O_{40}/TiO_2$ are estimated to be 2.73 eV, 3.06 eV, 3.08 eV, 2.91 eV and 2.86 eV, respectively.

The study of photocatalytic activity

The photocatalytic performances of synthetic materials are investigated by measuring the decomposition of RhB under simulated sunlight (320 nm $< \lambda <$ 780 nm). All photocatalytic activity tests are performed after the adsorption equilibrium is reached. In Fig. 6a, all catalysts reach adsorption equilibrium after 60 min in dark. The adsorption rates of g-CNQDs, P25, $H_3PW_{12}O_{40}/TiO_2$, 5% g-CNQDs/TiO_2, 3% g-CNQDs/$H_3PW_{12}O_{40}/TiO_2$, 5% g-CNQDs/$H_3PW_{12}O_{40}/TiO_2$ and 10% g-CNQDs/$H_3PW_{12}O_{40}/TiO_2$ are 13.2%, 11.2%, 11.7% 14.2%, 15.3%, 15.9% and 16.7%, respectively. The introduction of g-CNQDs enhances the adsorption capacity of $H_3PW_{12}O_{40}/TiO_2$ and raises specific surface area after compounding facilitates the capture of contaminants. Direct photolysis of RhB without addition of catalyst can be ignored. While under 30 min

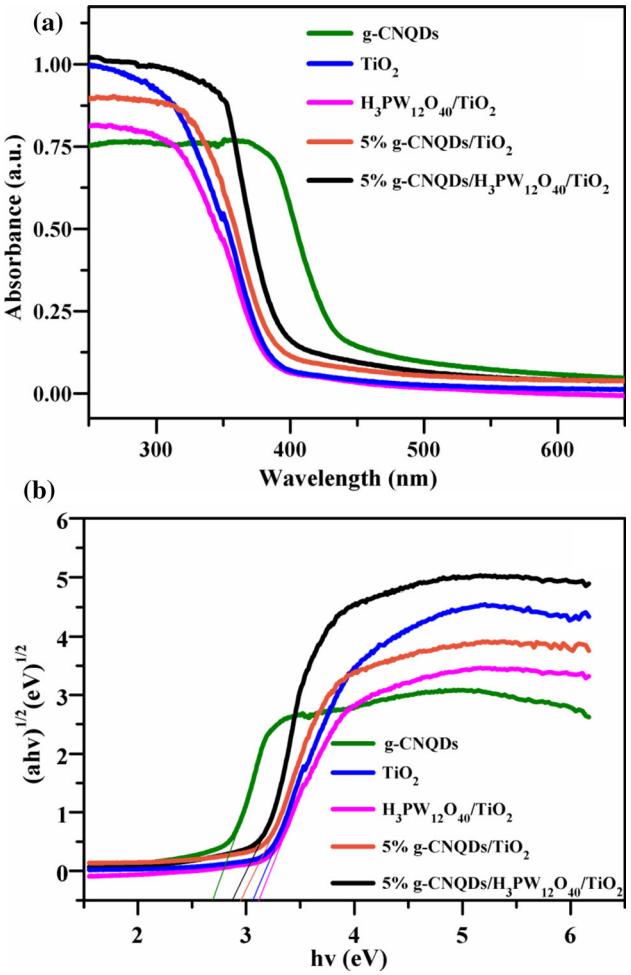

Figure 5 The UV–Vis DRS (**a**) and the bandgaps (**b**) of TiO_2, g-CNQDs, $H_3PW_{12}O_{40}/TiO_2$, 5% g-CNQDs/TiO_2, 5% g-CNQDs/$H_3PW_{12}O_{40}/TiO_2$, 10% g-CNQDs/$H_3PW_{12}O_{40}/TiO_2$.

simulated sunlight, g-CNQDs, P25, $H_3PW_{12}O_{40}/TiO_2$, 5% g-CNQDs/TiO_2, 10% g-CNQDs/$H_3PW_{12}O_{40}/TiO_2$, 3% g-CNQDs/$H_3PW_{12}O_{40}/TiO_2$ and 5% g-CNQDs/$H_3PW_{12}O_{40}/TiO_2$ exhibit degradation rates of 37.6%, 60.8%, 68.1%, 75.5%, 89.8%, 92.6% and 99.3% (Table 1), respectively. The photocatalytic performance of g-CNQDs/$H_3PW_{12}O_{40}/TiO_2$ composites exceeds that of g-CNQDs, P25, $H_3PW_{12}O_{40}/TiO_2$ and g-CNQDs/TiO_2. The degree of photocatalytic activity enhancement by ternary hybrids varies with the doping amount of g-CNQDs, and 5% g-CNQDs/$H_3PW_{12}O_{40}/TiO_2$ displays the highest efficiency of 99.3% during photodegradation of RhB. The corresponding RhB degradation first-order kinetic curve (Fig. 6b) indicates that the reaction rate constants of g-CNQDs, P25, $H_3PW_{12}O_{40}/TiO_2$, 5% g-CNQDs/TiO_2, 10% g-CNQDs/$H_3PW_{12}O_{40}/TiO_2$, 3% g-CNQDs/$H_3PW_{12}O_{40}/TiO_2$ and 5% g-CNQDs/$H_3PW_{12}O_{40}/TiO_2$ are 0.00927, 0.01863, 0.02243, 0.03036, 0.05291, 0.06363 and 0.10639 min^{-1} (Table 1), respectively. The degradation rate of 5% g-CNQDs/$H_3PW_{12}O_{40}/TiO_2$ is 11.48, 5.71, 4.74 and 3.51 times than that of g-CNQDs, P25, $H_3PW_{12}O_{40}/TiO_2$ and g-CNQDs/TiO_2, respectively. It can be observed that the apparent rate constant of g-CNQDs/$H_3PW_{12}O_{40}/TiO_2$ hybrid materials is significantly higher than the sum of g-CNQDs and $H_3PW_{12}O_{40}/TiO_2$. This may be due to the fact that g-CNQDs are loaded into $H_3PW_{12}O_{40}/TiO_2$, which produces a heterojunction that inhibits photoelectron–hole recombination and improves photocat-

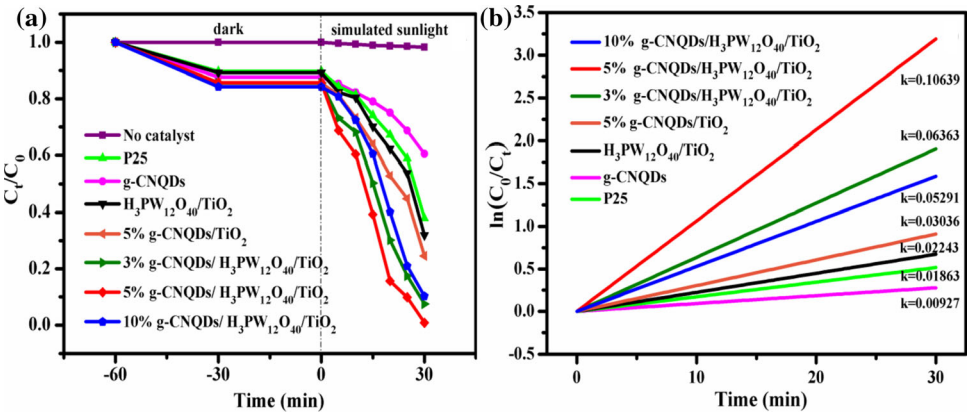

Figure 6 **a** Adsorption and photocatalytic properties of P25, g-CNQDs, $H_3PW_{12}O_{40}/TiO_2$, g-CNQDs/TiO_2, g-CNQDs/$H_3PW_{12}O_{40}/TiO_2$ toward degrading RhB under simulated sunlight (320 nm $< \lambda <$ 780 nm) irradiation. Catalyst content 50 mg, C_0 = 20 mg L^{-1}, volume 50 mL. **b** Various catalysts corresponding reaction constants of degrading RhB, C_0 is the initial concentration of contaminants.

Table 1 Degradation efficiency and apparent rate constant of RhB by photocatalysts

Photocatalyst	Degradation efficiency (%)	Apparent rate constant
g-CNQDs	37.6	0.00927
P25	60.8	0.01863
$H_3PW_{12}O_{40}/TiO_2$	68.1	0.02243
5% g-CNQDs/TiO_2	75.5	0.03036
10% g-CNQDs/$H_3PW_{12}O_{40}/TiO_2$	89.8	0.05291
3% g-CNQDs/$H_3PW_{12}O_{40}/TiO_2$	92.6	0.06363
5% g-CNQDs/$H_3PW_{12}O_{40}/TiO_2$	99.3	0.10639

alytic performance. It is notable that too much or too little g-CNQDs loading will not optimize the catalytic effect of g-CNQDs/$H_3PW_{12}O_{40}/TiO_2$ ternary composite. When the doping amount of g-CNQDs is high, it is harmful to photocatalytic activity. This phenomenon may be due to the fact that excess g-CNQDs act as a light shield, resulting in decreased photocatalytic activity [45].

Finally, visible-light (400 nm $< \lambda <$ 780 nm) photocatalytic activity of the TiO_2-based materials was studied, and the result is shown in Fig. S4. As shown in Fig. S4a, the 5% g-CNQDs/$H_3PW_{12}O_{40}/TiO_2$ composite still exhibited the highest visible-light photocatalytic degradation efficiency. Under 75 min visible light, g-CNQDs, P25, $H_3PW_{12}O_{40}/TiO_2$, 5% g-CNQDs/TiO_2, 10% g-CNQDs/$H_3PW_{12}O_{40}/TiO_2$, 3% g-CNQDs/$H_3PW_{12}O_{40}/TiO_2$ and 5% g-CNQDs/$H_3PW_{12}O_{40}/TiO_2$ displayed degradation rates of 36.4%, 51.2%, 58.7%, 70.2%, 93.6%, 98.5% and 99.2%, respectively. The apparent rate constant k (in Fig. S4b) over the g-CNQDs, P25, $H_3PW_{12}O_{40}/TiO_2$, 5% g-CNQDs/TiO_2, 10% g-CNQDs/$H_3PW_{12}O_{40}/TiO_2$, 3% g-CNQDs/$H_3PW_{12}O_{40}/TiO_2$ and 5% g-CNQDs/$H_3PW_{12}O_{40}/TiO_2$ is 0.00631, 0.01097, 0.01506, 0.02185, 0.03591, 0.04818 and 0.06226 min^{-1}, respectively. The degradation rate of 5% g-CNQDs/$H_3PW_{12}O_{40}/TiO_2$ was 9.86, 5.68, 4.13 and 2.85 times than that of g-CNQDs, P25, $H_3PW_{12}O_{40}/TiO_2$ and g-CNQDs/TiO_2, respectively. Consequently, the introduction of g-CNQDs significantly boosts the photocatalytic activity of $H_3PW_{12}O_{40}/TiO_2$.

Considering the practical applications, it is necessary to evaluate the stability and recyclability of 5% g-CNQDs/$H_3PW_{12}O_{40}/TiO_2$ sample during photocatalytic reaction. Hence, five consecutive RhB degradation cycles of g-CNQDs/$H_3PW_{12}O_{40}/TiO_2$ composite are carried under simulated sunlight irradiation (Fig. 7). After each experiment, the photocatalysts were recovered by filtration, and washed

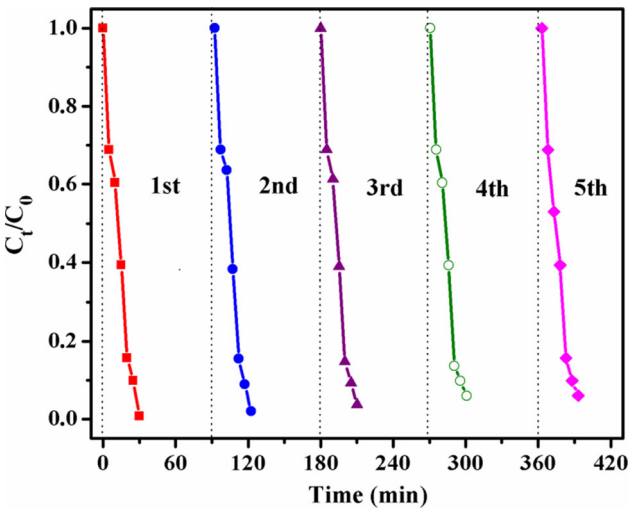

Figure 7 Recycling tests in degrading RhB for 5% g-CNQDs/$H_3PW_{12}O_{40}/TiO_2$ composite under simulated sunlight (320 nm $< \lambda <$ 780 nm) irradiation. Catalyst content 50 mg, C_0 = 20 mg L^{-1}, volume 50 mL.

three times with anhydrous ethanol and distilled water and dried at 80 °C for 12 h. In Fig. 7, the photocatalytic efficiency shows a trifling decline and there is no significant deactivation. The results confirmed that g-CNQDs/$H_3PW_{12}O_{40}/TiO_2$ can be regarded as a stable and effective heterogeneous photocatalyst in future applications.

In order to further prove the stability of the composites, TEM and XRD of g-CNQDs/$H_3PW_{12}O_{40}/TiO_2$ are studied after five cycles. As shown in Fig. S5, the TEM image of 5% g-CNQDs/$H_3PW_{12}O_{40}/TiO_2$ after 5 cycles is nearly the same as that of the original sample (Fig. 4c), which further demonstrates g-CNQDs/$H_3PW_{12}O_{40}/TiO_2$ is a stable recyclable photocatalyst. The XRD pattern of 5% g-CNQDs/$H_3PW_{12}O_{40}/TiO_2$ composites showed that the peak of g-CNQDs is very weak. In order to clearly observe the peak of g-CNQDs, XRD characterization is conducted for 10% g-CNQDs/$H_3PW_{12}O_{40}/TiO_2$ that after five cycles. As displayed in Fig. S6, the XRD

pattern of the sample after five cycles is nearly the same with that of the initial sample, demonstrating that the crystalline structure of g-CNQDs/$H_3PW_{12}O_{40}/TiO_2$ is not changed during the photocatalytic reaction. The result is also consistent with the research of Yan et al. [49, 50].

Probable photocatalytic mechanism of g-CNQDs/$H_3PW_{12}O_{40}/TiO_2$

Photoelectrochemistry (PEC) measurements are taken to disclose the transfer and separation situation of light-excited charge carriers among composite materials [51]. As shown in Fig. 8a, the photocurrent–time (*I–t*) curves are obtained on a membrane which has four switching periods under intermittent Xe illumination. It can be observed that the addition of $H_3PW_{12}O_{40}$ can enhance the photocurrent responses, whereas the photocurrent intensity of g-CNQDs/TiO_2 is higher than that of $H_3PW_{12}O_{40}/TiO_2$. It shows that g-CNQDs have a notable effect on photocatalytic activity enhancement. Moreover, 5% g-CNQDs/$H_3PW_{12}O_{40}/TiO_2$ displays the strongest photocurrent responses, indicating more efficient separation of photoinduced e^-–h^+ pairs, which can be achieved by corresponding photoluminescence (PL) results for further demonstration. Under 280 nm laser illumination at room temperature, different catalytic samples show a broad PL peak centered at around 382 nm (Fig. 8b). The PL intensity obtained on g-CNQDs/$H_3PW_{12}O_{40}/TiO_2$ is much lower than that of TiO_2, $H_3PW_{12}O_{40}/TiO_2$ and g-CNQDs/TiO_2, which means that the lifetime of photogenerated carriers in 5% g-CNQDs/$H_3PW_{12}O_{40}/TiO_2$ is longer.

To study the detailed band potentials, the valence band XPS spectra and Mott–Schottky plots were analyzed to estimate the band positions of TiO_2 and g-CNQDs, shown in Fig. S7. From Fig. S7a and b, it could be clearly seen that the flat band potentials of TiO_2 and g-CNQDs were − 0.89 V and − 0.83 V versus Ag/AgCl, respectively. Using the Nernst equation [47], the flat band potentials of TiO_2 and g-CNQDs were determined to be − 0.28 V and − 0.22 V versus NHE, respectively.

Moreover, as displayed in Fig. S7a and b, both slopes of the linear C^{-2} potential curves were positive, indicating that TiO_2 and g-CNQDs were the n-type materials. Since the flat band potential was approximately equivalent to the Fermi level of the n-type material [48], the Fermi level of TiO_2 was − 0.28 eV versus NHE and that of g-CNQDs was − 0.22 eV versus NHE. Furthermore, the valence band XPS spectra (Fig. S7c and d) revealed that the energy gaps between the valence band and the Fermi level were 3.16 eV and 1.84 eV for TiO_2 and g-CNQDs, respectively. Therefore, the valence band (VB) position of TiO_2 was calculated to equal to 2.88 eV. Combined with the bandgap value of TiO_2 (3.06 eV) which was obtained from Fig. 5, the conduction band (CB) position of TiO_2 was calculated as − 0.18 eV. Similarly, the CB position of g-CNQDs was calculated as − 1.11 eV.

In order to gain a deeper understanding of reaction mechanism, we studied the photoactive substances in the degradation process of organic contaminants over g-CNQDs/$H_3PW_{12}O_{40}/TiO_2$. The addition of ethylene diamine tetraacetic acid (EDTA), isopropanol (IPA) and 1,4-benzoquinone (BQ) plays the role of removing h^+_{VB}, $^{\cdot}OH$ and $^{\cdot}O_2^-$, respectively. It can be seen from Fig. 9 that after 30 min of BQ and IPA addition, the removal efficiency of RhB decreases by 42.7% and 30.8%, respectively. However, the removal efficiency changes slightly after adding EDTA. It is speculated that the dominant active species in the

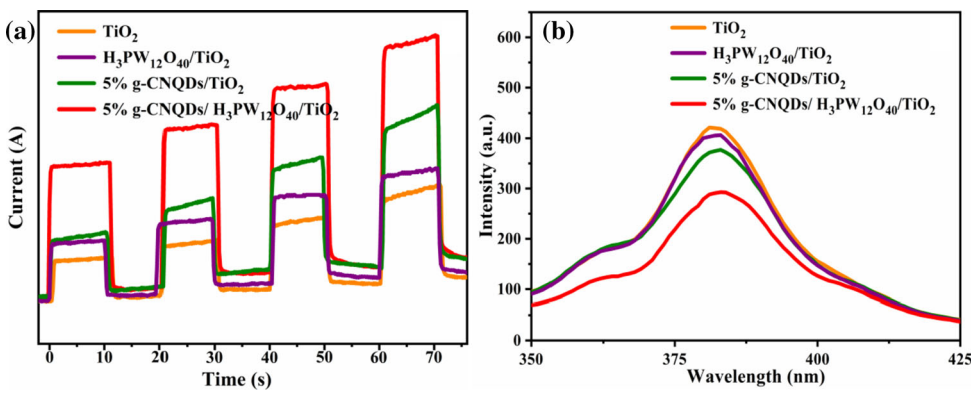

Figure 8 **a** Photocurrent tests of TiO_2, $H_3PW_{12}O_{40}/TiO_2$, 5% g-CNQDs/TiO_2, 5% g-CNQDs/$H_3PW_{12}O_{40}/TiO_2$ electrodes in Na_2SO_4 electrolyte solution under Xe illumination. **b** Various catalysts corresponding PL spectra under 280 nm laser illumination.

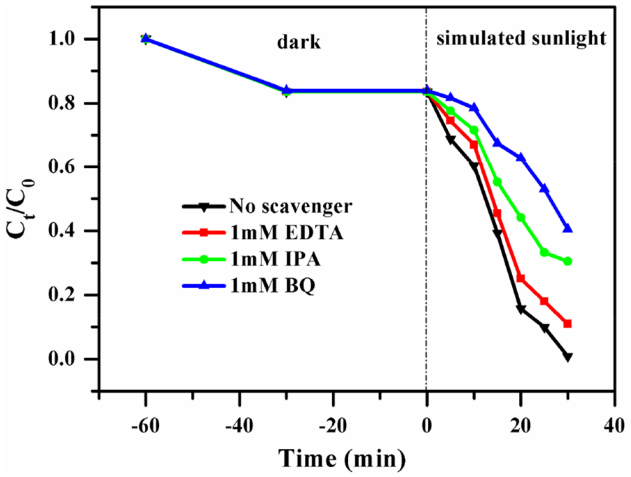

Figure 9 The influence of radical scavengers on catalytic performance of 5% g-CNQDs/$H_3PW_{12}O_{40}$/TiO_2 for degrading RhB under simulated sunlight (320 nm < λ < 780 nm) irradiation. Catalyst content 50 mg, C_0 = 20 mg L^{-1}, volume 50 mL.

photocatalytic process of g-CNQDs/$H_3PW_{12}O_{40}$/TiO_2 are $\cdot O_2^-$ and $\cdot OH$, and the holes as an adjunct.

Discussion

Based on the results of photocatalytic experiments and trapping oxidants tests, a possible photocatalytic mechanism for the g-CNQDs/$H_3PW_{12}O_{40}$/TiO_2 is proposed and schematically exhibited in Scheme 1. Given the calculation results from XPS, the CB edge potentials for $H_3PW_{12}O_{40}$, TiO_2 and g-CNQDs are 0.22 eV, − 0.18 eV and − 1.11 eV, whereas those of VB are 3.70 eV, 2.88 eV and 1.62 eV, respectively. Under simulated sunlight irradiation, both g-CNQDs and TiO_2 can be excited to generate electron–hole pairs because of the bandgap energy of g-CNQDs (2.73 eV) and TiO_2 (3.06 eV). The CB edge of TiO_2 is more negative than that of $H_3PW_{12}O_{40}$; the photoinduced electrons on TiO_2 to the CB of $H_3PW_{12}O_{40}$, h^+ remain on the VB of TiO_2 and g-CNQDs. The e^- on the CB of $H_3PW_{12}O_{40}$ tends to recombine with the h^+ on the VB of g-CNQDs. These transfers would diminish photoinduced carriers' recombination and extend service life of charges. At the same time, e^-_{CB} that transferred onto the catalyst surface also reacted with oxygen molecules absorbed onto the catalyst surface to generate $\cdot O_2^-$ and $\cdot OH$. Additionally, the h^+ on VB of TiO_2 could oxidize OH^- or H_2O to produce $\cdot OH$. Subsequently, the active species with strong oxidizing properties, including $\cdot O_2^-$, $\cdot OH$ and h^+_{VB}, generated in the g-CNQDs/$H_3PW_{12}O_{40}$/TiO_2 photocatalytic system can bring the speedy transformation of organic dyes into inorganic compounds with the assistance of simulated sunlight. The detail response equations were shown from Eqs. (1) to (6).

It is apparent that the g-CNQDs/$H_3PW_{12}O_{40}$/TiO_2 ternary system exhibits enhanced photodegradation ability for the following reasons. Initially, the introduction of g-CNQDs can reduce bandgap energy and boost solar energy utilization of $H_3PW_{12}O_{40}$/TiO_2, which is easy to produce more h^+_{VB} and e^-_{CB}. Meanwhile, the up-conversion properties of g-CNQDs converts' long-wave illumination light into shorter-wavelength emission light, which allows it to be further utilized in composite materials. Moreover, the increased specific surface area of g-CNQDs/$H_3PW_{12}O_{40}$/TiO_2 ternary material facilitates the adsorption of contaminants. Suitable band structure alignment and efficient electron transport among

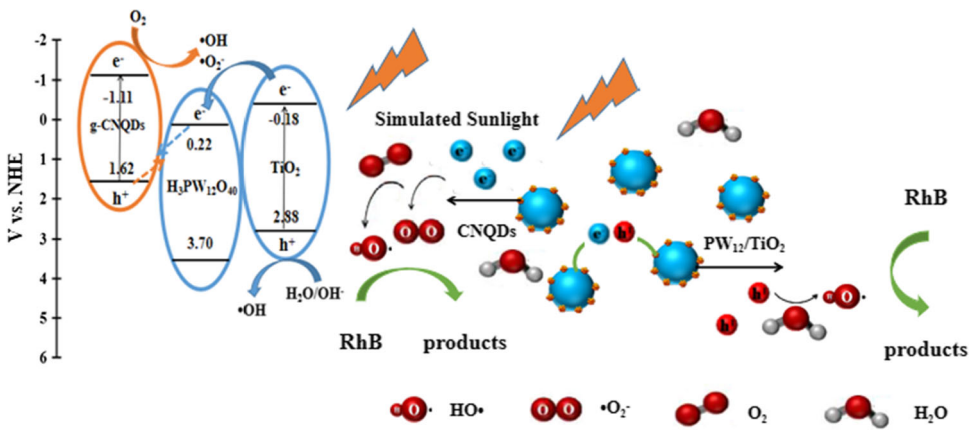

Scheme 1 Mechanism schematic of photocatalytic degradation of RhB over simulated sunlight illuminating g-CNQDs/$H_3PW_{12}O_{40}$/TiO_2 ternary heterostructure.

distinct photocatalysts are key factors in the formation of heterojunctions to boost electron transfer capability.

$$CNQDs/PW_{12}/TiO_2 \xrightarrow{\text{simulated sunlight}} CNQDs/PW_{12}/TiO_2(h^+_{VB}+e^-_{CB}) \quad (1)$$

$$O_2 + e^-_{CB} \rightarrow {}^{\cdot}O_2^- \quad (2)$$

$$O_2 + 2H^+ + 3e^-_{CB} \rightarrow {}^{\cdot}OH + OH^- \quad (3)$$

$$h^+_{VB} + OH^- \rightarrow {}^{\cdot}OH \quad (4)$$

$$h^+_{VB} + H_2O \rightarrow {}^{\cdot}OH + H^+. \quad (5)$$

Studies have shown that g-CNQDs/$H_3PW_{12}O_{40}$/TiO_2 still has efficient photoactivity after five cycling runs and is considered as a potent and stable photocatalyst driven by sunlight.

Acknowledgements

This work was financially supported by Science and Technology Development Plan of Jilin Province (20180520081JH) and Thirteen Five-Year Program for Science and Technology of Education Department of Jilin Province (JJKH20200803KJ, JJKH20200804KJ).

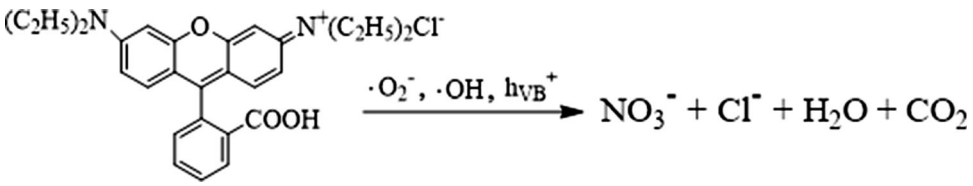

(6)

Conclusion

A new high-efficiency ternary composite photocatalyst g-CNQDs/$H_3PW_{12}O_{40}$/TiO_2 is obtained via coupling g-CNQDs with $H_3PW_{12}O_{40}$/TiO_2 by ultrasonic method. The results show that the g-CNQDs/$H_3PW_{12}O_{40}$/TiO_2 with 5% g-CNQDs loaded possesses the highest photocatalytic activity under simulated sunlight. The splendid photocatalytic performance probably originates from: (1) The matched bandgap position between the three materials effectively facilitates separation and migration of photogenerated electron–hole, thus enhancing the quantum efficiency. (2) The loading of g-CNQDs broadens the photoresponsive region of $H_3PW_{12}O_{40}$/TiO_2, and the up-conversion effect of g-CNQDs increases UV-light intensity, thereby increasing photon efficiency of the system. (3) The introduction of g-CNQDs raises the specific surface area of the ternary composite material and then increases the active sites of the reaction. (4) In the $H_3PW_{12}O_{40}$/TiO_2 reaction system, the active species are ${}^{\cdot}O_2^-$ and h^+_{VB}. For g-CNQDs/$H_3PW_{12}O_{40}$/TiO_2, the active species are not only ${}^{\cdot}O_2^-$ and h^+_{VB} but also ${}^{\cdot}OH$, which is also the direct evidence of doping g-CNQDs to improve the degradation efficiency of pollutants.

Electronic supplementary material: The online version of this article (https://doi.org/10.1007/s10853-020-05083-7) contains supplementary material, which is available to authorized users.

References

[1] Li Z, Che GB, Jiang W, Liu LH, Wang HR (2019) Visible-light-driven CQDs@MIL-125(Ti) nanocomposite photocatalyst with enhanced photocatalytic activity for the degradation of tetracycline. RSC Adv 9:33238–33245

[2] Singh RK, Kumar R, Singh DP, Savu R, Moshkalev SA (2019) Progress in microwave-assisted synthesis of quantum dots (graphene/carbon/semiconducting) for bioapplications: a review. Mater Today Chem 12:282–314

[3] Kumar R, Sahoo S, Joanni E, Singh RK, Tan WK, Kar KK, Matsuda A (2019) Recent progress in the synthesis of graphene and derived materials for next generation electrodes of high performance lithium ion batteries. Prog Energy Combust Sci 75:100786

[4] Kumar R, Joanni E, Singh RK, Singh DP, Moshkalev SA (2018) Recent advances in the synthesis and modification of carbon-based 2D materials for application in energy conversion and storage. Prog Energy Combust Sci 67:115–157

[5] Kumar R, Matsuo R, Kishida K, Abdel-Galeil MM, Suda Y, Matsuda A (2019) Homogeneous reduced graphene oxide supported NiO–MnO_2 ternary hybrids for electrode material with improved capacitive performance. Electrochim Acta 303:246–256

[6] Linsebigler AL, Lu G, Yates JT (1995) Photocatalysis on TiO_2 surfaces: principles, mechanisms, and selected results. Chem Rev 95:735–758

[7] Daghrir R, Drogui P, Robert D (2013) Modified TiO_2 for environmental photocatalytic applications: a review. Ind Eng Chem Res 52:3581–3599

[8] Gaya UI, Abdullah AH (2008) Heterogeneous photocatalytic degradation of organic contaminants over titanium dioxide: a review of fundamentals, progress and problems. J Photochem Photobiol C Photochem Rev 9:1–12

[9] Zhang J, Zhou DD, Dong SS, Ren NQ (2019) Respective construction of Type-II and direct Z-scheme heterostructure by selectively depositing CdS on 001 and 101 facets of TiO_2 nanosheet with CDots modification: a comprehensive comparison. J Hazard Mater 366:311–320

[10] Yoon JW, Kim DH, Kim JH, Jang HW, Lee JH (2019) NH_2-MIL-125(Ti)/TiO_2 nanorod heterojunction photoanodes for efficient photoelectrochemical water splitting. Appl Catal B Environ 244:511–518

[11] Lu ZY, Chen F, He M, Song MS, Ma ZF, Shi WD, Yan YS, Lan JZ, Li F (2014) Xiao, Microwave synthesis of a novel magnetic imprinted TiO_2 photocatalyst with excellent transparency for selective photodegradation of enrofloxacin hydrochloride residues solution, chem. Eng. J. 249:15–26

[12] Yi J, Yuan X, Wang H, Yu H, Peng F (2015) Preparation of $Bi_2Ti_2O_7$/TiO_2 nanocomposites and their photocatalytic performance under visible light irradiation. Mater Des 86:152–155

[13] Wang JB, Liu C, Yang S, Lin X, Shi WL (2020) Fabrication of a ternary heterostructure $BiVO_4$ quantum dots/C60/g-C_3N_4 photocatalyst with enhanced photocatalytic activity. J Phys Chem Solids 136:109164

[14] Fu J, Tian YL, Chang BB, Xi FN, Dong XP (2012) BiOBr-carbon nitride heterojunctions: synthesis, enhanced activity and photocatalytic mechanism. J Mater Chem 22:21159–21166

[15] Zhang XD, Wang HX, Wang H, Zhang Q, Xie JF, Tian YP, Wang J (2014) Single-layered graphitic-C_3N_4 quantum dots for two-photon fluorescence imaging of cellular nucleus. Adv Mater 26:4438–4443

[16] Tang YR, Su YY, Yang N, Zhang LC, Lv Y (2014) Carbon nitride quantum dots: a novel chemiluminescence system for selective detection of free chlorine in water. Anal Chem 86:4528–4535

[17] Kumar R, Silva ETSG, Singh RK, Savu R, Alaferdov AV, Fonseca LC, Carossi LC, Singh A, Khandka S, Kar KK, Alves OL, Kubota LT, Moshkalev SA (2018) Microwave-assisted synthesis of palladium nanoparticles intercalated nitrogen doped reduced graphene oxide and their electrocatalytic activity for direct-ethanol fuel cells. J Colloid Interface Sci 515:160–171

[18] Kumar R, Savu R, Singh RK, Joanni E, Singh DP, Tiwari VS, Vaz AR, Silva ETSG, Maluta JR, Kubota LT, Moshkalev SA (2017) Controlled density of defects assisted perforated structure in reduced graphene oxide nanosheets-palladium hybrids for enhanced ethanol electro-oxidation. Carbon 117:137–146

[19] Kumar R, Singh RK, Singh DP, Joanni E, Yadav RM, Moshkalev SA (2017) Laser-assisted synthesis, reduction and micro-patterning of graphene: recent progress and applications. Coord Chem Rev 342:34–79

[20] Kumar R, Kim HJ, Park S, Srivastava A, Oh IK (2014) Graphene-wrapped and cobalt oxide-intercalated hybrid for extremely durable super-capacitor with ultrahigh energy and power densities. Carbon 79:192–202

[21] Barman S, Sadhukhan M (2012) Facile bulk production of highly blue fluorescent graphitic carbon nitride quantum dots and their application as highly selective and sensitive sensors for the detection of mercuric and iodide ions in aqueous media. J Mater Chem 22:21832

[22] Wang WJ, Yu JC, Shen Z, Chan DKL, Gu T (2014) g-C_3N_4 quantum dots: direct synthesis, upconversion properties and photocatalytic application. Chem Commun 50:10148–10150

[23] Wang XP, Wang LX, Zhao F, Hu CG, Zhao Y, Zhang ZP, Chen SL, Shi GQ, Qu LT (2015) Monoatomic-thick graphitic carbon nitride dots on graphene sheets as an efficient catalyst in the oxygen reduction reaction. Nanoscale 7:3035–3042

[24] Lin X, Liu C, Wang JB, Yang S, Shi JY, Hong YZ (2019) Graphitic carbon nitride quantum dots and nitrogen-doped carbon quantum dots co-decorated with $BiVO_4$ microspheres: a ternary heterostructure photocatalyst for water purification. Sep Purif Technol 226:117–127

[25] Su JY, Zhu L, Chen GH (2016) Ultrasmall graphitic carbon nitride quantum dots decorated self-organized TiO_2 nanotube arrays with highly efficient photoelectrochemical activity. Appl Catal B Environ 186:127–135

[26] Hiskia A, Mylonas A, Papaconstantinou E (2001) Comparison of the photoredox properties of polyoxometallates and semiconducting particles. Chem Soc Rev 30:62–69

[27] Taghavi M, Ehrampoush MH, Ghaneian MT, Tabatabaee M, Fakhri Y (2018) Application of a Keggin-type heteropoly acid on supporting nanoparticles in photocatalytic

degradation of organic pollutants in aqueous solutions. J Clean Prod 197:1447–1453

[28] Lu N, Lu Y, Liu FY, Zhao K, Yuan X, Zhao YH, Li Y (2013) $H_3PW_{12}O_{40}/TiO_2$ catalyst-induced photodegradation of bisphenol A (BPA): kinetics, toxicity and degradation pathways. Chemosphere 91:1266–1272

[29] Li LJ, Li L, Sun TT, Yu XM, Long L, Xu L, Yan JH (2019) Novel $H_3PW_{12}O_{40}/TiO_2$-g-C_3N_4 type-II heterojunction photocatalyst with enhanced visible-light photocatalytic properties. J Solid State Chem 274:152–161

[30] Malengreaux CM, Pirard SL, Léonard G, Mahy JG, Herlitschke M (2017) Study of the photocatalytic activity of Fe^{3+}, Cr^{3+}, La^{3+} and Eu^{3+} single-doped and co-doped TiO_2 catalysts produced by aqueous sol–gel processing. J Alloys Compd 691:726–738

[31] Song ZP, Lin TR, Lin LH, Lin S, Fu FF, Wang XC, Guo LQ (2016) Invisible security ink based on water-soluble graphitic carbon nitride quantum dots. Angew Chem Int Ed 128:2823–2827

[32] He L, Dong YN, Zheng Y, Jia QM, Shan SY, Zhang YQ (2019) A novel magnetic MIL-101(Fe)/TiO_2 composite for photodegradation of tetracycline under solar light. J Hazard Mater 361:85–94

[33] Yin Y, Zhang YM, Gao TL, Yao T, Han J, Han ZB, Zhang ZH (2017) One-pot evaporation–condensation strategy for green synthesis of carbon nitride quantum dots: an efficient fluorescent probe for ion detection and bioimaging. Mater Chem Phys 194:293–301

[34] Lu YC, Chen J, Wang AJ, Bao N, Feng JJ, Wang WP, Shao LX (2015) Facile synthesis of oxygen and sulfur co-doped graphitic carbon nitride fluorescent quantum dots and their application for mercury (II) detection and bioimaging. J Mater Chem C 3:73–78

[35] Zhang Q, Quan X, Wang H, Chen S, Su Y, Li ZL (2017) Constructing a visible-light-driven photocatalytic membrane by g-C_3N_4 quantum dots and TiO_2 nanotube array for enhanced water treatment. Sci Rep 7:3128

[36] Lin X, Wang YS, Zheng J, Liu C, Yang Y, Che GB (2016) Graphitic carbon nitride quantum dots loaded on leaf-like $InVO_4/BiVO_4$ nanoheterostructures with enhanced visible-light photocatalytic activity. J. Alloys Compd 688:891–898

[37] He JJ, Sun HQ, Indrawirawan S, Duan XG, Tade MO, Wang SB (2015) Novel polyoxometalate@g-C_3N_4 hybrid photocatalysts for degradation of dyes and phenolics. J Colloid Interface Sci 456:15–21

[38] Taghavi M, Ehrampoush MH, Ghaneian MT, Tabatabaee M, Fakhri Y (2007) Photocatalytic degradation of textile dye X-3B using polyoxometalate-TiO_2 hybrid materials. J Hazard Mater 141:123–127

[39] Fan XQ, Feng Y, Su YY, Zhang LC, Lv Y (2015) A green solid-phase method for preparation of carbon nitride quantum dots and their applications in chemiluminescent dopamine sensing. RSC Adv 5:55158–55164

[40] Li H, Shao FQ, Huang H, Feng JJ, Wang AJ (2016) Eco-friendly and rapid microwave synthesis of green fluorescent graphitic carbon nitride quantum dots for vitro bioimaging. Sens Actuators B Chem 226:506–511

[41] Gao HC, Wu XN, Sun DM, Niu GL, Guan JY, Meng XF (2019) Preparation of core–shell $PW_{12}@TiO_2$ microspheres and oxidative desulfurization performance. Dalton Trans 48:5749–5755

[42] Wu YC, Ju LS (2014) Annealing-free synthesis of C–N Co-doped TiO_2 hierarchical spheres by using amine agents via microwave-assisted solvothermal method and their photocatalytic activities. J Alloys Compd 604:164–170

[43] Xu L, Yang X, Guo Y, Ma F, Guo Y, Yuan X, Huo M (2010) Simulated sunlight photodegradation of aqueous phthalate esters catalyzed by the polyoxotungstate/titania nanocomposite. J Hazard Mater 178:1070–1077

[44] Lu N, Wang YQ, Ning SQ, Zhao WJ, Qian M, Ma Y, Wang J (2017) Design of plasmonic Ag–$TiO_2/H_3PW_{12}O_{40}$ composite film with enhanced sunlight photocatalytic activity towards o-chlorophenol degradation. Sci Rep 7:17298

[45] Li Y, Wu S, Huang L, Wang J, Xu H, Li H (2014) Synthesis of carbon-doped g-C_3N_4 composites with enhanced visible-light photocatalytic activity. Mater Lett 137:281–284

[46] Sun M, Wang Y, Fang Y, Sun S, Yu Z (2016) Construction of $MoS_2/CdS/TiO_2$ ternary composites with enhanced photocatalytic activity and stability. J Alloys Compd 684:335–341

[47] Rengifo-Herrera JL, Blanco M, Wist J, Florian P (2016) TiO_2 modified with polyoxotungstates should induce visible-light absorption and high photocatalytic activity through the formation of surface complexes. Appl Catal B Environ 189:99–109

[48] Lu ZY, Peng JY, Song MS, Liu Y, Liu XL, Huo PW, Dong HJ, Yuan SQ, Ma ZF, Han S (2019) Improved recyclability and selectivity of environment-friendly MFA-based heterojunction imprinted photocatalyst for secondary pollution free tetracycline orientation degradation. Chem Eng J 360:1262–1276

[49] Lu ZY, Yu ZH, Dong JB, Song MS, Liu Y, Liu XL, Ma ZF, Su H, Yan YS, Huo PW (2018) Facile microwave synthesis of a Z-scheme imprinted $ZnFe_2O_4$/Ag/PEDOT with the specific recognition ability towards improving photocatalytic activity and selectivity for tetracycline. Chem Eng J 337:228–241

[50] Lu ZY, Zhu Z, Wang DD, Ma ZF, Shi WD, Yan YS, Zhao XX, Dong HJ, Yang L, Hua ZF (2016) Specific oriented recognition of a new stable ICTX@Mfa with retrievability

for selective photocatalytic degrading of ciprofloxacin. Catal Sci Technol 6:1367–1377

[51] Li JJ, Weng B, Cai SC, Chen J, Jia HP, Xu YJ (2018) Efficient promotion of charge transfer and separation in hydrogenated TiO_2/WO_3 with rich surface-oxygen-vacancies for photodecomposition of gaseous toluene. J Hazard Mater 342:661–669